Surface Science 605 (2011) 333–340

Contents lists available at ScienceDirect

Surface Science

journal homepage: www.elsevier.com/ locate/susc

Surface electronic and structural properties of nanostructured titanium oxide grown by pulsed laser deposition

M. Fusi [a], E. Maccallini [b], T. Caruso [b], C.S. Casari [a,f,*], A. Li Bassi [a,f], C.E. Bottani [a,f], P. Rudolf [c], K.C. Prince [d,e], R.G. Agostino [b]

[a] Dipartimento di Energia and NEMAS-Center for NanoEngineered MAterials and Surfaces, Politecnico di Milano, Via Ponzio, 34/3 I-20133 Milano, Italy
[b] CNISM-Dipartimento di Fisica, Università della Calabria, Ponte Bucci, Cubo 33c, I-87036 Arcavacata di Rende (CS), Italy
[c] Zernike Institute for Advanced Materials, University of Groningen, Nijenborgh 4, NL-9747 AG, Groningen, Netherlands
[d] Sincrotrone Trieste, S.S. 14 km 163.5, in Area Science Park, I-34012 Basovizza, Trieste, Italy
[e] Istituto Officina dei Materiali, Consiglio Nazionale delle Ricerche, Area Science Park, I-34149 Trieste, Italy
[f] Center for Nano Science and Technology CNST of IIT@PoliMI, Via Pascoli, 70/3 I-20133 Milano, Italy

ARTICLE INFO

Article history:
Received 4 August 2010
Accepted 25 October 2010
Available online 30 October 2010

Keywords:
Titanium dioxide
Surface structure and defects
Pulsed laser deposition PLD
Electron spectroscopy UPS
XPS
X-ray absorption spectroscopy XAS
NEXAFS
Synchrotron radiation

ABSTRACT

Titanium oxide nanostructured thin films synthesized by pulsed laser deposition (PLD) were here characterized with a multi-technique approach to investigate the relation between surface electronic, structural and morphological properties. Depending on the growth parameters, these films present characteristic morphologies ranging from compact to columnar and to an extremely open structure. As-deposited films have a disordered structure both in the bulk and on the surface, as shown by Raman spectroscopy and by the fine structure of X-ray absorption spectra near the Ti and O edge (NEXAFS). The surface reactivity towards the atmosphere, with consequent formation of surface hydroxyl terminal groups, turns out to be dependent not only on the effective surface but also on the surface structure. By ultraviolet photoemission spectroscopy, we observed that, depending on the sample structure and morphology, defect states at 1 eV binding energy in the valence band can be induced by exposing the samples to the intense synchrotron photon beam.
After annealing in air at 673 K, the structural order increases towards a mainly anatase phase in which the presence of rutile increases in films with a more open morphology. Such structural modifications influence the surface stability since the defect formation in the valence band is strongly reduced in all the annealed films, and it is completely hindered in the most compact films.

1. Introduction

Titanium dioxide (TiO_2) is a widely investigated material which has been successfully employed in many applications ranging from self-cleaning surfaces to electronics, energy and biotechnology [1,2]. For such applications the TiO_2 surface electronic and structural properties are crucial: the presence of oxygen vacancies can affect the interaction with water in that it favours H_2O dissociation and formation of hydroxyl groups [3,4], or modify the photocatalytic properties [5,6], or alter the interaction with organic molecules [7].

Nanostructuring TiO_2 can provide beneficial effects as for instance in photocatalytic properties or in superhydrophilic behaviour even without the need of UV irradiation, thus resulting in systems with enhanced performances [1,8–10]. Hence engineering the nanostructure and understanding how the surface electronic properties are related to the structure are of paramount importance in an applied technology context.

In this framework pulsed laser deposition (PLD) is a particularly attractive technique since it allows production of nanostructured films with tailored features. By ablating in the presence of a background gas, cluster formation is favoured and the kinetic energy of the deposited particles is reduced [11–13], thus allowing the synthesis of cluster-assembled films with an accurate control of morphology and structure [9,14,15]. Exploiting this approach, nanostructured TiO_2 films showing interesting properties for biotechnology [8], photocatalytic [9] and photovoltaic [16] applications have been recently produced.

In the literature many studies devoted to the investigation of electronic and structural properties of TiO_2 single crystalline surfaces [2] have been reported, while there is a much smaller number of studies of nanostructured TiO_2 [17–26]. Even fewer reports describe explicitly the relationship [18,19,23–25] between different morphologies and corresponding surface electronic and structural properties.

In the present work, we aim to get a comprehensive picture of the surface properties of nanostructured TiO_2 films obtained by PLD at

* Corresponding author.
E-mail address: carlo.casari@polimi.it (C.S. Casari).

0039-6028/$ – see front matter © 2010 Elsevier B.V. All rights reserved.
doi:10.1016/j.susc.2010.10.039

room temperature in different oxidizing and inert background atmospheres and optionally annealed to tune their morphology and structure. These films consist of nano-aggregates (10–20 nm) ranging from amorphous to anatase and rutile phases assembled in compact or open morphologies which differ on the 10–100 nm scale [9].

Since the role of the surface properties such as structure, defects and stability, as well as surface contamination due to interaction with the atmosphere, is of particular interest for the above mentioned applications, we studied these surface properties under conditions close to those of applications. To avoid possible modifications due to cleaning procedures, films were measured *ex situ* without any further *in situ* treatment. In addition titanium metallic films were deposited to compare the effect of oxidation caused by exposure to the ambient atmosphere when the samples are extracted from the deposition chamber. Films characterized by a different morphology at the nanoscale have been investigated by means of *ex-situ* X-ray/UV photoelectron spectroscopy (XPS and UPS) at a synchrotron radiation facility. We monitored the presence of surface defects (i.e., oxygen vacancies) and of chemisorbed species (water molecules, organic contaminants and hydroxyl groups). The degree of crystalline order in the film surface was evaluated by near edge X-ray absorption fine structure (NEXAFS) and compared with complementary information coming from Raman spectroscopy. This cross linked analysis permits correlation of the structural properties arising from the nanoscale sizing with the corresponding surface electronic features and with the properties of the conduction and valence states close to the Fermi edge.

2. Experimental

Titanium oxide films were grown by PLD on Si(100) and Al substrates at room temperature exploiting UV laser pulses (duration ≈10–15 ns) from a KrF excimer laser ($\lambda = 248$ nm, 10 Hz repetition rate) focused on a Ti target (purity 99.99%) with an energy density (fluence) of about 3 J/cm^2. The deposition chamber was equipped with a multiple gas inlet system, allowing control of the gas composition and variation of the pressure from high vacuum (10^{-6} Pa base pressure) to atmospheric pressure. Films of ~200 nm thickness were grown with a target-to-substrate distance of 50 mm. Ar:O_2 — 4:1 mixture and pure Ar were employed as background gases during deposition and the total pressure was varied in the range between 10 and 60 Pa. The Ar:O_2 mixture was chosen to simulate synthetic air where Ar has been used instead of N_2 to avoid possible formation of nitrides. Post-deposition thermal treatment at 673 K was performed for 1 h in a muffle furnace in air. The temperature was chosen to induce structural ordering without inducing a phase transition from anatase to rutile. After the preparation, samples were

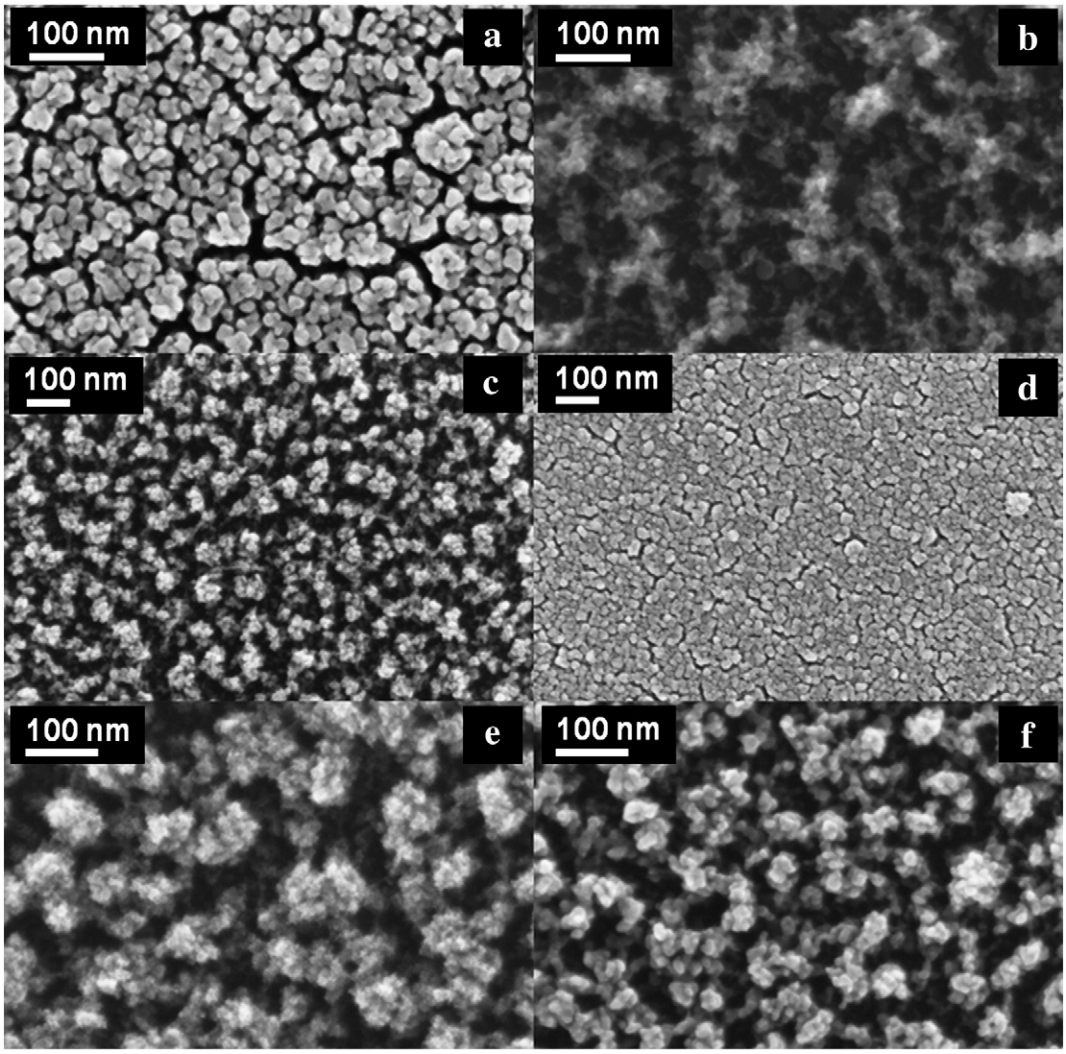

Fig. 1. Scanning electron microscopy images of titanium oxide films deposited by PLD: a) and b) comparison at the same magnification of samples deposited in Ar:O_2 atmosphere at 10 Pa (a) and 60 Pa (b); c) and d) comparison at the same magnification of samples deposited at 30 Pa in Ar:O_2 (c) and Ar (d) atmosphere; e) and f) comparison at the same magnification of samples deposited in Ar:O_2 at 30 Pa before (e) and after (f) the annealing treatment at 673 K in air for 1 h. The size bar corresponds to 100 nm.

either characterized immediately or stored in static vacuum until the measurements with the synchrotron light source could be performed.

SEM images were acquired with a Zeiss Supra 40 field emission scanning electron microscope. AFM images were collected in tapping mode with an Autoprobe CP II Research (Thermomicroscope) microscope in air using silicon tips with radius <10 nm (Nanosensors). Film density was evaluated by comparing deposited mass measured by a quartz microbalance with film thickness measured by cross sectional SEM. Visible Raman spectra were acquired with a Renishaw InVia spectrometer using the 514.5 nm wavelength of an argon ion laser. XPS, UPS and NEXAFS measurements were performed at the Material Science beamline at the Elettra synchrotron light source equipped with a plane grating monochromator [27] and a Specs Phoibos 150 mm hemispherical analyzer. No cleaning treatments were performed before acquiring normal emission photoelectron spectra at 650 eV photon energy with an overall spectral resolution of 0.5 eV. UPS data were collected at 50 eV and 200 eV photon energies with an overall energy resolution of 0.1 eV. Binding energies were referenced to the Au *4f* core level emission spectra. The XPS spectra were normalized to the incoming photon flux and a standard curve fitting analysis (mixed Gaussian–Lorentzian lineshape) was performed to identify the different components. NEXAFS spectra were acquired in Auger electron yield mode at the Ti $L_{2,3}$ and O *K* edges with a photon energy resolution of 0.1 eV. Calibration of the absorption spectra was carried out by measuring the photon energy using the Au *4f* core lines excited with first order light. Curve fitting analysis was performed with Winspec™ software.

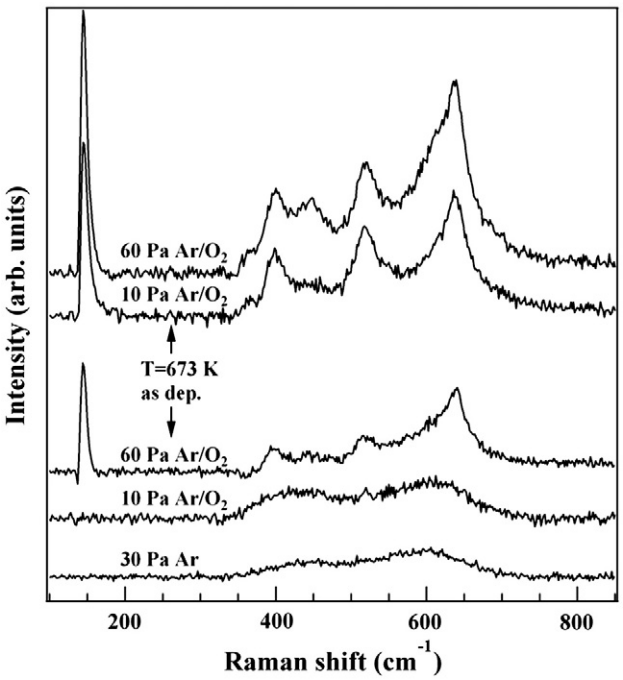

Fig. 2. Raman spectra of titanium oxide films deposited by PLD in Ar:O_2 atmosphere (10 Pa and 60 Pa), before and after annealing at 673 K in air for 1 h. The spectrum of the as-deposited film produced in Ar atmosphere at 30 Pa is also shown.

3. Results and discussion

3.1. Morphology and crystalline structure

Fig. 1a–d shows SEM images of films grown in Ar and Ar:O_2 gases at different pressures (10–60 Pa). By increasing the Ar:O_2 pressure we obtain films from compact and dense (Fig. 1a), to porous and columnar (at 30 Pa, Fig. 1c) morphology. At higher pressure the samples are porous with an extremely open morphology (60 Pa, Fig. 1b). Such porous systems with a high effective surface are composed of nanoparticles (size of about 10–20 nm) assembled in a hierarchical or disordered arrangement depending on the deposition pressure, as revealed by SEM and TEM images reported in previous works [9,16]. As a consequence the density decreases approximately from a maximum of ~2 g/cm^3 to a minimum ≤0.4 g/cm^3 and the porosity correspondingly increases from 45% to more than 90%, as shown in previous work [9]. The surface roughness (root mean square roughness measured by AFM, images not shown) increases from 4.4 ± 0.2 nm to 13.2 ± 0.4 nm by increasing the deposition pressure from 10 Pa to 30 Pa. The effective surface evaluated from analysis of 1 × 1 μm^2 AFM images increases from 1.1 μm^2 at 10 Pa to 1.6 μm^2 at 60 Pa.

The film grown in a pure Ar background atmosphere at 30 Pa (see Fig. 1d) is even denser and smoother (2.5 ± 0.4 nm rms surface roughness) than the one grown at 10 Pa Ar:O_2. When ablating in an inert gas, only scattering of the ablated species takes place while no chemical reactions occur, leading to a different kinetic energy and temperature of the deposited species [28]. For the as-deposited samples, the Raman spectra presented in Fig. 2 are characterized by broad bands indicating a disordered titanium oxide structure for the film deposited at 10 Pa, while at 60 Pa Raman peaks typical of the crystalline anatase phase start to appear [29]. Although the most intense anatase peak at 144 cm^{-1} is evident, other peaks belonging to the anatase phase at 399, 529 and 639 cm^{-1} are not well defined and constitute an unresolved structure, indicating the coexistence of a disordered phase. Moreover, these wide bands could mask the two main peaks of rutile at 440 and 612 cm^{-1}, and thus the simultaneous presence of the rutile phase cannot be excluded *a priori*. Interestingly, also the as-deposited sample produced in a 30 Pa pure Ar atmosphere presents a Raman spectrum with broad bands typical of disordered TiO_2. Since the film is 200 nm thick and the Raman cross section from disordered TiO_2 is usually low, we can conclude that the oxidation, which occurs once the sample is removed from the growth chamber and exposed to air, may be favoured by the porous morphology and involves the film internal structure and not only the surface. None of the Raman spectra showed any quantum confinement effects (i.e. blue shift and broadening of the anatase peak at 144 cm^{-1}) which generally start to become visible for particle size below ~10 nm [30].

For all samples thermal treatment increases the crystalline order [9] while the morphology and the surface roughness are not significantly modified (see Fig. 1E and F). Nanoparticles constituting the nanostructured assembly increase their crystalline order without coalescing or growing in size. This is also supported by XRD measurements, reported in ref. [9], showing the presence of ordered grains with typical size changing from about 20 nm to 10 nm by increasing the pressure from 10 to 100 Pa. From the Raman spectra reported in Fig. 2, the main crystalline phase of the annealed samples is still anatase, identified by the peak at 144 cm^{-1}. Other peaks typical for anatase at 399, 529 and 639 cm^{-1} are still not completely resolved and for samples grown at higher pressures (≥30 Pa), features at 447 and 612 cm^{-1} appear, which indicate also the presence of the rutile phase [31].

3.2. Surface composition and electronic properties

3.2.1. Core level photoemission spectra

Selected Ti *2p*, O *1s* and C *1s* core level XPS spectra are reported in Fig. 3 (see Supplementary Information for the complete set of spectra as well as the curve fitting analysis).

All the investigated samples show the same Ti *2p* spectra (see Fig. 3(a)), characterized by spin-orbit (1/2, 3/2) Ti^{4+} doublet components at 458.8 eV and 464.4 eV binding energy [2,18,32–35]. No Ti^{3+} shoulder at lower binding energy on the Ti $2p_{3/2}$ peak was detected, suggesting that all samples have a stoichiometric surface [33]. In the O *1s* spectra (see Fig. 3(b)) three contributions can be discerned for all

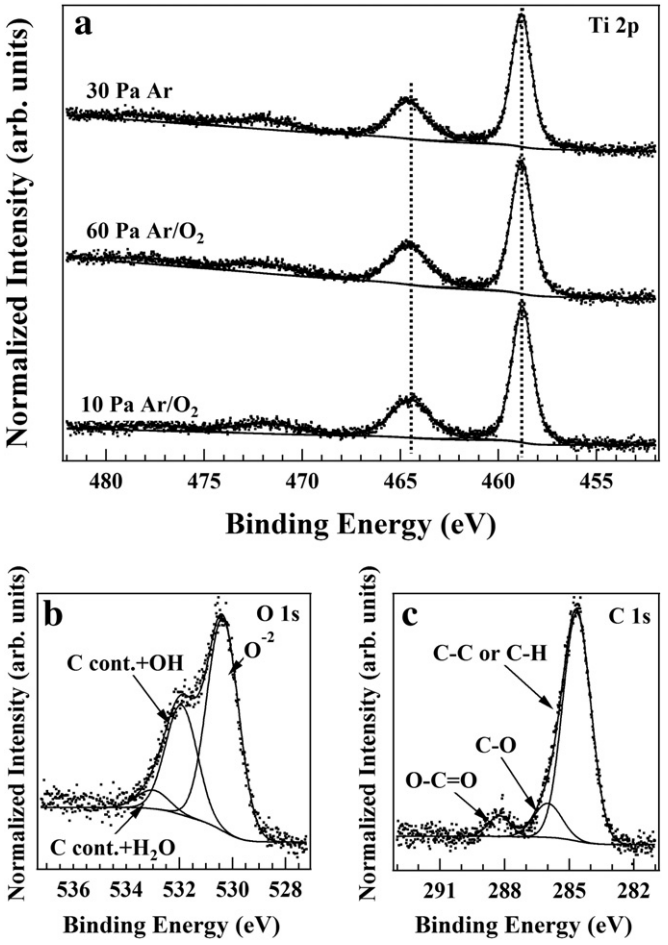

Fig. 3. (a) Photoemission spectra and relative fitting curves of the Ti *2p* core level region for titanium oxide films deposited by PLD in Ar:O_2 atmosphere (10 Pa or 60 Pa) and Ar atmosphere (30 Pa). Photoemission spectra and relative fitting curves of the C *1s* (b) and O *1s* (c) core level regions for a film deposited in Ar:O_2 atmosphere at 10 Pa.

samples; one at ~530.4 eV binding energy due to the O^{2-} oxygen species of titanium dioxide, [33] one at ~532.1 eV assigned to (Ti bonded) OH^- hydroxyl oxygen and/or to C–O and O–C=O species coming from organic contaminants (the signal of hydroxyl groups cannot be distinguished from that of C–O and O–C=O since they have similar binding energies) [36,37], while the one at ~533 eV may be due to adsorbed water molecules or to ester oxygen in a carboxyl group [33,37]. The main observable trend (see Table 1) among the as-deposited samples is an increase of organic contamination/hydroxyl oxygen and water uptake with increasing Ar:O_2 pressure during deposition. This behaviour can be attributed not only to the higher surface area but also to a higher surface reactivity, as discussed in Section 3.3.

Table 2
Intensity of the C *1s* main component at 284.6 eV in the XPS spectra of the titanium oxide thin films before and after 673 K thermal annealing (the intensity is normalized to that of the Ti $2p_{3/2}$ XPS peak, the error is 0.01).

TiO_2 film deposited in	C *1s* (284.6 eV)/Ti $2p_{3/2}$ intensity ratio	
	As deposited	Annealed
10 Pa Ar:O_2	0.82	0.81
30 Pa Ar:O_2	2.23	1.29
60 Pa Ar:O_2	2.28	1.45
30 Pa Ar	1.85	=

Annealing does not modify the O *1s* signals of the samples synthesized in Ar:O_2 atmosphere. On the contrary, the contamination and OH^- signal of the sample synthesized in pure Ar atmosphere decreases after thermal treatment, probably related to the high reactivity of the metallic surface to oxygen, water and organic contaminants by air exposure, resulting in a larger amount of chemisorbed organic contaminants/OH^- groups.

At the same time, C *1s* spectra (see Fig. 3(c)) can be fitted with three contributions at 284.6 eV, 286.2 eV and 288.2 eV binding energy and assigned to C–C/C–H, C–O and O–C=O groups [37]. The C *1s* signals (see Table 2) increase with the pressure during deposition in both the as-deposited and the annealed samples, while at a given pressure the annealing treatment reduces the intensity of the carbon signal. For the sample deposited in Ar atmosphere, the C *1s* intensity is slightly reduced compared to the sample deposited in Ar:O_2 (at the same pressure) but higher compared to the one deposited in 10 Pa Ar:O_2. Although it is not possible solely from the O *1s* spectra to distinguish between OH groups bound to Ti and contaminant species, the ratio between the intensities of O *1s* signal due to contaminants and OH groups (532.1 eV) and the sum of the oxygen-bonded C *1s* components (286.2 eV and 288.2 eV), reported in Fig. 4, can give some hints about the OH groups present on the surface. This ratio increases a) with the deposition pressure and b) upon annealing for samples deposited in 30 and 60 Pa of Ar:O_2 atmosphere. This behaviour may be explained by partial removal of C-containing contaminants and substitution with hydroxyl groups bonded to Ti surface after annealing [38]. Moreover, the sample synthesized in 30 Pa pure Ar presents a higher intensity ratio compared to samples grown in 10 Pa and 30 Pa Ar:O_2 atmosphere, in agreement with the general observation that a partially oxidized Ti surface shows enhanced reactivity towards OH groups.

3.2.2. Valence band photoemission spectra

Fig. 5(a) shows valence band photoemission spectra before and after the annealing procedure. At a photon energy of $h\nu = 50$ eV the photoelectron escape depth is nearly 4Å [39] and the spectra are therefore very sensitive to the electronic properties of the topmost surface layer. In agreement with previous studies [2,18,40], we assign the intense features located between 3.5 eV and 10 eV binding energy to O *2p*–Ti *3d* hybridized states. These two overlapping features correspond to different O *2p*–Ti *3d* hybridizations: the feature at 7 eV

Table 1
Percentage of oxygen signal coming from Ti and/or from adsorbed species calculated by fitting the O *1s* core level regions in the XPS spectra of titanium oxide thin films before and after 673 K thermal annealing (see text).

TiO_2 film deposited in	**O**$^{2-}$ (%)		(Ti)–**O**–H; C–**O**; **O**–C=**O** (%)		H_2**O**$_{ads}$; O–C=O (%)	
	O *1s* signal at 530.4 eV		O *1s* signal at 532.1 eV		O *1s* signal at 533.0 eV	
	As deposited	Annealed	As deposited	Annealed	As deposited	Annealed
10 Pa Ar:O_2	80 ± 1	80 ± 1	20 ± 1	20 ± 1	–	–
30 Pa Ar:O_2	70 ± 3	70 ± 1	25 ± 2	25 ± 1	5 ± 1	5 ± 1
60 Pa Ar:O_2	62 ± 1	63 ± 1	32 ± 1	30 ± 1	6.0 ± 0.5	7.0 ± 0.5
30 Pa Ar	66 ± 1	74 ± 1	30 ± 1	22 ± 1	4 ± 1	4 ± 1

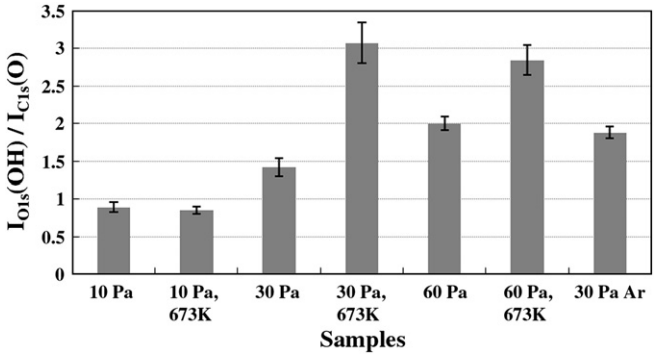

Fig. 4. Intensity ratio of the O *1s* XPS signal due to OH and the C *1s* XPS signal of carbon bonded to oxygen atoms (see text for details).

contains a higher Ti *3d* contribution while the 5 eV feature has mainly O *2p* character [40].

All the as-deposited samples grown in Ar:O_2 atmospheres show a broad signal around 10.5 eV, the intensity of which scales with the deposition pressure. The sample grown at 30 Pa in pure Ar presents instead a much more intense feature, which has a completely different shape and is shifted to higher binding energy by nearly 0.5 eV. According to the literature, the 3σ orbital of OH^- is responsible for a *VB* spectral feature at a binding energy of ~10.8 eV [41] and organic contaminants can introduce an extra feature at ~11 eV [42]. In agreement with the analysis of the C *1s* and O *1s* core level spectra reported above, this difference confirms that the oxidation process, occurring exclusively in air for the sample grown in pure Ar, leads to a higher amount of organic contaminants and/or of hydroxyl groups. After annealing, the intensity of the feature at ~11 eV disappears in this sample, indicating desorption of organic contaminants bonded to the surface. The intensity increase of the ~10.5 eV binding energy feature with Ar:O_2 pressure is in agreement with the intensity enhancement of the O *1s* component (OH^-/organic contaminants) in the XPS spectra.

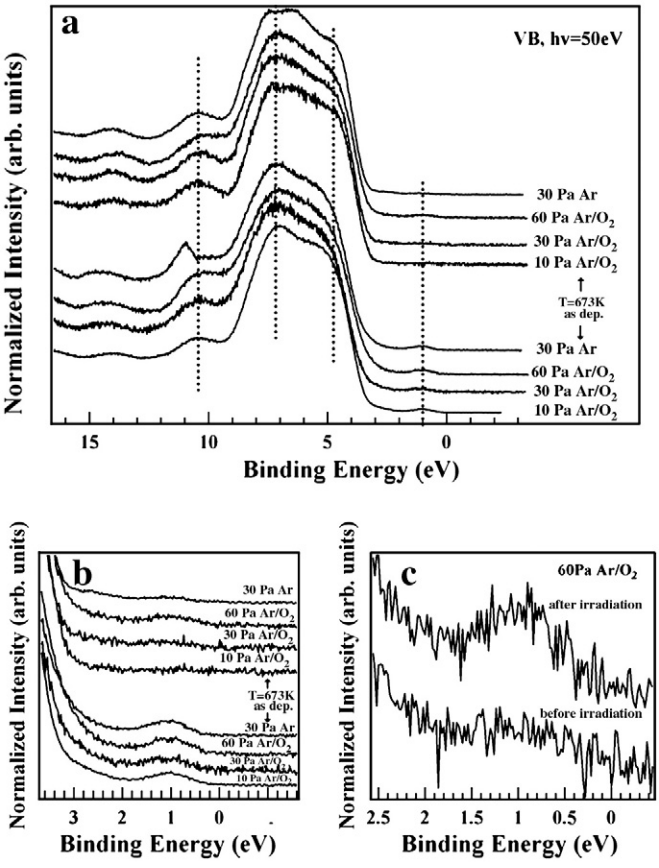

Fig. 5. (a) Valence band photoemission spectra ($h\nu = 50$ eV) for titanium oxide films deposited by PLD in a 10 Pa, 30 Pa or 60 Pa Ar:O_2 atmosphere or in 30 Pa pure Ar, before and after annealing in air at 673 K for 1 h. (b) Fermi edge region of the valence band spectra. (c) Detail of the defect-induced band before and after irradiation with 50 eV photons.

In the as-deposited samples we observe the presence of a feature at ~1 eV below E_F (see Fig. 5(b)) generally attributed to substoichiometric Ti^{3+} ions [2,43]. The nature of this reduced state is still controversial since both Ti interstitials and oxygen vacancies give rise to spectral intensity at ~1 eV binding energy [3,44]. Interestingly, we observed that in our case the presence of the defect state is induced by irradiation (see Fig. 5(c)) since the defect state appears after irradiating the same region for some minutes with a flux of about 10^{15} photons s^{-1} cm^{-2}. This defect-induced effect is not observed in the Ti *2p* core levels, probably because of the different photon flux (30–40 times lower) and the lower surface sensitivity when using a photon energy equal to 650 eV. Since the peak at ~1 eV is radiation induced, we believe that it is mainly due to oxygen vacancies and not to Ti interstitials. Vacancies may form by local excitation, local heating and irradiation by secondary electrons [45], which cause oxygen desorption [46] and/or removal of less stably bonded hydroxyl groups [47]. In annealed samples the surface seems to be more stable and defect-induced state forms only for the film grown at the highest pressure (60 Pa in Ar:O_2) (see Fig. 5(b)).

3.2.3. NEXAFS analysis of titanium and oxygen edges

The local symmetry and the electronic environment of the titanium oxide surface have been investigated by X-ray absorption spectroscopy at the Ti $L_{2,3}$ and O *K*–edges as shown in Fig. 6. Typically, the Ti $L_{2,3}$ absorption spectra of TiO_2 present four main peaks related to transitions from the Ti *2p* core levels to the t_{2g}^* and e_g^* orbitals which are affected by the oxygen ligands' crystal field and hence by the different ligand configurations and local distortions [2].

In particular the e_g^* states possess a large degree of hybridization and are very sensitive to the Ti atom local environment: sharp peaks occur in crystalline samples and the L_3-e_g^* band is further split into two sub-bands (Fig. 6c); more precisely in anatase the lower photon energy component of the L_3-e_g^* peak is more intense than the higher photon energy one, while the opposite is true in rutile [22]. Broader e_g^* peaks occur in disordered materials (see Fig. 6(a)) (in our case, in samples with smaller grain size) and are attributed to distortions and random variations of bond angles and lengths.

Correspondingly the O *K*-edge absorption spectrum shows two main features at ~531 eV and ~534 eV (marked E and F in Fig. 6(b) and (d)). These peaks are due to excitations from O *1s* levels to the t_{2g}^* and e_g^* orbitals of TiO_2; the unresolved structures at higher photon energy are due to transitions to antibonding bands derived from the covalent mixing of O *2p* and Ti *4sp* states [48]. The energy difference between the t_{2g}^* and e_g^* features (E–F) at the O *K*-edge spectra is commonly used as an estimate of the crystal field splitting strength and amounts to ~3.0 eV in rutile and to 2.8 eV in anatase whereas it is reduced to 2.3 eV in disordered samples [22]. The crystal field splitting of the O *K*-edge bands reported in Fig. 6 increases from ~1.8 eV (as-deposited samples) to 2.5 eV (annealed samples). This splitting in the as-deposited sample is then lower than that observed for TiO_2 aerogels [22] (2.3 eV) and this may be due to higher disorder in the coordination of the oxygen ligands and to a weaker Ti *3d*–O *2p* hybridization [49]. In the case of annealed samples, this splitting is lower compared to the single crystal structure but higher than for the aerogel sample.

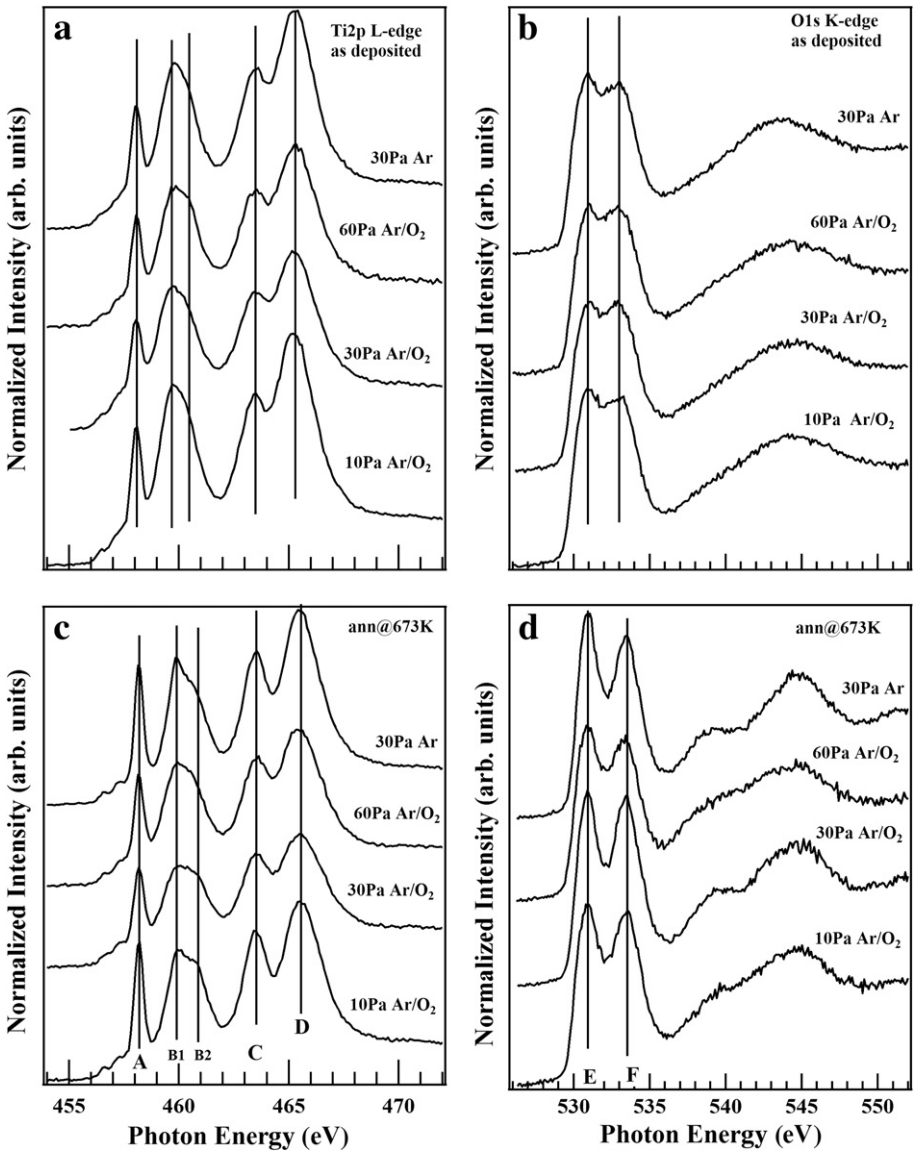

Fig. 6. Near edge X-ray absorption fine structure (NEXAFS) spectra of titanium oxide thin films deposited by PLD in a 10 Pa, 30 Pa or 60 Pa Ar:O_2 atmosphere or in 30 Pa pure Ar, collected at the Ti L_{23} edge as deposited (a) and after annealing in air at 673 K for 1 h (c). The t_{2g}^* and e_g^* related peaks at the L_3 edge are labeled A and B, while the corresponding ones at the L_2 edge are labeled C and D. NEXAFS spectra at the O *K* edge for as deposited films (b) and after annealing in air at 673 K for 1 h (d).

The Ti $L_{2,3}$ edge NEXAFS spectra (see Fig. 6(a) and (c)) give a more detailed knowledge and reveal further differences on the samples. The results of the curve fitting analysis of the Ti $L_{2,3}$ edge NEXAFS spectra are presented in Table 3. The spectra were fitted by mixed Gaussian/Lorentzian peaks: (i) two pre-edge features at $h\nu = 456.5$ eV and $h\nu = 457.5$ eV, (ii) one t_{2g}^* "A" peak at $h\nu \sim 458$ eV and (iii) two peaks (e_g^* B1, e_g^* B2) to reproduce the e_g^* "B" band; the corresponding peaks at the L_2 edge were fitted in an analogous fashion. The results (see Table 3) clearly point to a transition to a crystalline phase after annealing at 673 K for some samples, namely the samples deposited in 10 Pa Ar:O_2 and 30 Pa Ar atmosphere. For these samples, the B1 peak becomes narrower: a difference of 0.3 eV (10 Pa Ar:O_2) and 0.4 eV (30 Pa Ar) after annealing. Concurrently the t_{2g}^* and e_g^* B2 peaks' intensities increase (by ~30%) after annealing at 673 K, while the e_g^* B1 peak decreases. In the 60 Pa sample instead, differences before and after annealing are almost absent, while the behaviour of the 30 Pa Ar:O_2 sample is intermediate between the 10 Pa and 60 Pa suggesting a partial phase transition.

Since the t_{2g}^* and e_g^* B2 peaks are related to the crystalline order while the e_g^* B1 peak is more related to the remaining disordered phase [50], the intensity enhancement of the former (in 10 Pa Ar:O_2 and 30 Pa Ar) supports local ordering of TiO_2 at the surface after annealing. In particular, the shape of the Ti L_3-e_g^* peak confirms that the local surface symmetry and ligand coordination are typical of the anatase phase in the annealed samples, while the samples produced in 30 and 60 Pa Ar:O_2 are less ordered.

Further differences emerge comparing samples deposited at different pressures: with increasing pressure during deposition, the relative intensity of the L_3-t_{2g}^*-related feature decreases compared to the relative intensity of the L_3-e_g^* B1 peak, pointing to lower local symmetry or higher concentration of defects. This agrees also with the observed lower L_3-e_g^* peak splitting and generally broader peaks for higher pressures during film growth. This trend is more marked in the annealed samples, indicating a greater difference in local surface order.

3.3. Discussion

With the help of O *1s* and *VB* photoemission spectra as well as NEXAFS spectra, we have highlighted differences depending on the pressure during deposition, the background gas composition, and the temperature treatment; considering all the presented experimental

Table 3
Curve fitting analysis of the Ti L_3 edge with three main peaks which reproduce the t_{2g}^* (A peak) and the two e_g^* peaks (B1 and B2 peaks). The full width at half maximum and the relative intensity of the peaks are reported (width uncertainty is 0.1 eV and intensity uncertainty is <5%).

Sample peaks	10 Pa Ar:O_2	10 Pa Ar:O_2 annealed at 673 K	30 Pa Ar:O_2	30 Pa Ar:O_2 400 °C	60 Pa Ar:O_2	60 Pa Ar:O_2 annealed at 673 K	30 Pa Ar	30 Pa Ar annealed at 673 K
t_{2g}^* width (eV)	0.6	0.5	0.6	0.6	0.6	0.6	0.6	0.5
t_{2g}^* relative intensity (%)	18	23	13	21	18	19	18	22
e_g^* B1 width (eV)	1.5	1.2	1.5	1.5	1.5	1.50	1.5	1.1
e_g^* B1 relative intensity (%)	55	38	52	45	47	50	55	39
e_g^* B2 width (eV)	1.5	1.5	1.5	1.5	1.5	1.5	1.5	1.5
e_g^* B2 relative intensity (%)	28	39	29	34	35	30	27	39

data, we can draw a comprehensive picture of the relation between surface electronic and structural properties and the nanostructure of TiO_2 films grown by PLD.

A comparison with literature results shows that as-deposited samples present NEXAFS features similar to amorphous TiO_2 or to titania aerogels. Comparison with Raman data provides complementary information compared to NEXAFS since it probes the internal film structure and it is sensitive to the structural order on a longer range. The Raman signal from small crystalline domains of the anatase phase increases for samples produced in a high background pressure, while on the surface the bond angles and lengths are very disordered, as evidenced by NEXAFS. As expected, after annealing the local order at the surface is increased, in particular for denser films (i.e., films deposited in lower background pressures), even though the NEXAFS peaks are broader than for single crystalline surfaces, indicating a residual variation in local bond angles and lengths [22]. The higher surface local ordering is related to easier nano-crystalline grain formation in compact films, as supported also by XRD data [9]. The Raman spectrum of annealed films is dominated by more resolved anatase-type peaks and, for samples produced in high background pressures, there is also a weak rutile signal. This suggests the presence of small rutile grains buried below a surface layer of atoms with a weak anatase-type coordination, as evidenced by NEXAFS.

We observe that defects are more easily induced on as-deposited samples than on annealed surfaces, and that even with less marked differences, samples deposited at lower pressures show a higher stability towards photon induced defects. The surface stability is improved in surfaces with a higher structural order as shown by NEXAFS.

The surface structure has a leading role in the interaction with OH and contaminants. Of course also the film morphology has a profound effect on the surface properties but the increase in the effective surface area alone cannot account for the observed variations of OH/contaminants. In fact, in as-deposited samples a ~1.5-fold increase of surface area (obtained from analysis of the AFM images) is observed when changing from 10 to 60 Pa deposition pressure, and this leads to an approximately 2-fold rise of the intensity due to organic contaminants/OH^- in the XPS O *1s* spectra (normalized to the Ti *2p* intensity), and an even higher increase of the main C *1s* signal. As expected, samples deposited in a higher background pressure have a larger surface area available to host or trap molecules; however, the dissociation of water and organic molecules is favoured at oxygen vacancies [32,51,52] and some studies point to the fact that, compared to single crystals, nanostructured surfaces include a higher amount of native defects, which are saturated through air exposure [10,19,53]. The importance of native defects is underlined by the samples deposited in 30 Pa of pure Ar. In this case, despite its more compact and smoother morphology, the surface is certainly more defective as suggested by the higher C–O/OH^- contribution in the O *1s* and C1s core levels, and by the intense peak at ~11 eV in the *VB* photoemission spectrum, indicating that it is more hydroxylated. This implies that the surface structure (i.e., the presence of defects) determines the density of contaminants, more than the morphology itself. The annealing procedure strongly influences the surface reactivity leading to an increase in grafted hydroxyl radicals. This mechanism, explained as a removal of organic contaminants (probably saturating defects sites) and replacement with OH groups, may influence the wettability properties required for superhydrophilicity [38].

4. Conclusions

Exploiting synchrotron-based spectroscopy and microscopy techniques, we investigated the surface structure of TiO_x thin films characterized by varying morphology and structural order at the nanoscale. The morphology (density and roughness of the sample), which can be tuned in the PLD process by changing the deposition parameters, is not affected by annealing, while structural and surface electronic properties are significantly modified. Moreover, when the sample is more compact and smooth, annealing enhances the local ordering and the stability under photon beam irradiation, as shown by the lower density of photon-induced defect states in the valence band spectra.

This complete characterization of the morphological, electronic and structural properties allows us to understand what governs the surface properties of TiO_x thin films. The nanoscale morphology and porosity together with structure, and the presence of surface defects determine the amount and type of hydroxyl group and/or organic contamination. This may in turn significantly affect surface properties relevant for a wide range of applications in which surface mediated processes have a key role, such as photocatalytic activity, wettability properties and interaction with organic and biological molecules (e.g. dyes, polymers and proteins) that are of technological interest for developing materials and systems such as self-cleaning [9] and anti-fog surfaces, dye sensitized or hybrid photovoltaic devices [16] and biosensors [8].

Acknowledgements

F.D.F., C.S.C, C.E.B. and A.L.B. acknowledge funding from Fondazione Cariplo (project n.2009/2527 “Nanostructured MATerials for innovative HYbrid Solar cells — MATHYS”).

Appendix A. Supplementary data

Supplementary data to this article can be found online at doi:10.1016/j.susc.2010.10.039.

References

[1] X. Chen, S.S. Mao, Titanium dioxide nanomaterials: synthesis, properties, modifications, and applications, Chemical Reviews 107 (2007) 2891–2959.
[2] U. Diebold, The surface science of titanium dioxide, Surface Science Reports 48 (2003) 53–229.
[3] S. Wendt, P.T. Sprunger, E. Lira, G.K.H. Madsen, Z.S. Li, J.O. Hansen, J. Matthiesen, A. Blekinge-Rasmussen, E. Laegsgaard, B. Hammer, F. Besenbacher, The role of interstitial sites in the Ti3d defect state in the band gap of Titania, Science 320 (2008) 1755–1759.

[4] R. Schaub, R. Thostrup, N. Lopez, E. Laegsgaard, I. Stensgaard, J.K. Norskov, F. Besenbacher, Oxygen vacancies as active sites for water dissociation on rutile TiO2 (110), Physical Review Letters 87 (2001).
[5] A. Fujishima, X.T. Zhang, D.A. Tryk, TiO2 photocatalysis and related surface phenomena, Surface Science Reports 63 (2008) 515–582.
[6] H.H. Lo, N.O. Gopal, S.C. Ke, Origin of photoactivity of oxygen-deficient TiO2 under visible light, Applied Physics Letters 95 (2009).
[7] G.J. Fleming, H. Idriss, Probing the reaction pathways of DL-proline on TiO2(001) single crystal surfaces, Langmuir 20 (2004) 7540–7546.
[8] F. Torta, M. Fusi, C.S. Casari, C.E. Bottani, A. Bachi, Titanium dioxide coated MALDI plate for on target analysis of phosphopeptides, Journal of Proteome Research 8 (2009) 1932–1942.
[9] F. Di Fonzo, C.S. Casari, V. Russo, M.F. Brunella, A.L. Bassi, C.E. Bottani, Hierarchically organized nanostructured TiO2 for photocatalysis applications, Nanotechnology 20 (2009).
[10] E. Hosono, H. Matsuda, I. Honma, M. Ichihara, H. Zhou, Synthesis of a perpendicular TiO2 nanosheet film with the superhydrophilic property without UV irradiation, Langmuir 23 (2007) 7447–7450.
[11] A. Bailini, F. Di Fonzo, M. Fusi, C.S. Casari, A. Li Bassi, V. Russo, A. Baserga, C.E. Bottani, Pulsed laser deposition of tungsten and tungsten oxide thin films with tailored structure at the nano- and mesoscale, Applied Surface Science 253 (2007) 8130–8135.
[12] D.H. Lowndes, D.B. Geohegan, A.A. Puretzky, D.P. Norton, C.M. Rouleau, Synthesis of novel thin-film materials by pulsed laser deposition, Science 273 (1996) 898–903.
[13] D. Cattaneo, S. Foglio, C.S. Casari, A. Li Bassi, M. Passoni, C.E. Bottani, Different W cluster deposition regimes in pulsed laser ablation observed by in situ scanning tunneling microscopy, Surface Science 601 (2007) 1892–1897.
[14] M. Fusi, V. Russo, C.S. Casari, A.L. Bassi, C.E. Bottani, Titanium oxide nanostructured films by reactive pulsed laser deposition, Applied Surface Science 255 (2009) 5334–5337.
[15] F. Di Fonzo, A. Bailini, V. Russo, A. Baserga, D. Cattaneo, M.G. Beghi, P.M. Ossi, C.S. Casari, A.L. Bassi, C.E. Bottani, Synthesis and characterization of tungsten and tungsten oxide nanostructured films, Catalysis Today 116 (2006) 69–73.
[16] F. Sauvage, F. Di Fonzo, A. Li Bassi, C.S. Casari, V. Russo, G. Divitini, C. Ducati, C.E. Bottani, P. Comte, M. Graetzel, Hierarchical TiO2 photoanode for dye-sensitized solar cells, Nano Letters 10 (2010) 2562–2567.
[17] M. Walczak, E.L. Papadopoulou, M. Sanz, A. Manousaki, J.F. Marco, M. Castillejo, Structural and morphological characterization of TiO2 nanostructured films grown by nanosecond pulsed laser deposition, Applied Surface Science 255 (2009) 5267–5270.
[18] T. Caruso, C. Lenardi, R.G. Agostino, M. Amati, G. Bongiorno, T. Mazza, A. Policicchio, V. Formoso, E. Maccallini, E. Colavita, G. Chiarello, P. Finetti, F. Sutara, T. Skala, P. Piseri, K.C. Prince, P. Milani, Electronic structure of cluster assembled nanostructured TiO2 by resonant photoemission at the Ti L-2,L-3 edge, Journal of Chemical Physics 128 (2008).
[19] T. Caruso, C. Lenardi, T. Mazza, A. Policicchio, G. Bongiorno, R.G. Agostino, G. Chiarello, E. Colavita, P. Finetti, K.C. Prince, C. Ducati, P. Piseri, P. Milani, Photoemission investigations on nanostructured TiO2 grown by cluster assembling, Surface Science 601 (2007) 2688–2691.
[20] K. Schwanitz, U. Weiler, R. Hunger, T. Mayer, W. Jaegermann, Synchrotron-induced photoelectron spectroscopy of the dye-sensitized nanocrystalline TiO2/electrolyte interface: band gap states and their interaction with dye and solvent molecules, Journal of Physical Chemistry C 111 (2007) 849–854.
[21] A. Orendorz, J. Wusten, C. Ziegler, H. Gnaser, Photoelectron spectroscopy of nanocrystalline anatase TiO2 films, Applied Surface Science 252 (2005) 85–88.
[22] S.O. Kucheyev, T. van Buuren, T.F. Baumann, J.H. Satcher, T.M. Willey, R.W. Meulenberg, T.E. Felter, J.F. Poco, S.A. Gammon, L.J. Terminello, Electronic structure of titania aerogels from soft X-ray absorption spectroscopy, Physical Review B 69 (2004).
[23] H.C. Choi, H.J. Ahn, Y.M. Jung, M.K. Lee, H.J. Shin, S.B. Kim, Y.E. Sung, Characterization of the structures of size-selected TiO2 nanoparticles using X-ray absorption spectroscopy, Applied Spectroscopy 58 (2004) 598–602.
[24] T.L. Hanley, V. Luca, I. Pickering, R.F. Howe, Structure of titania sol–gel films: a study by X-ray absorption spectroscopy, Journal of Physical Chemistry B 106 (2002) 1153–1160.
[25] V. Luca, S. Djajanti, R.F. Howe, Structural and electronic properties of sol–gel titanium oxides studied by X-ray absorption spectroscopy, Journal of Physical Chemistry B 102 (1998) 10650–10657.
[26] E.C.H. Sykes, M.S. Tikhov, R.M. Lambert, Surface composition, morphology, and catalytic activity of model polycrystalline Titania surfaces, Journal of Physical Chemistry B 106 (2002) 7290–7294.
[27] R. Vasina, V. Kolarik, P. Dolezel, M. Mynar, M. Vondracek, V. Chab, J. Slezak, C. Comicioli, K.C. Prince, Mechanical design aspects of a soft X-ray plane grating monochromator, Nuclear Instruments & Methods in Physics Research Section a-Accelerators Spectrometers Detectors and Associated Equipment 467 (2001) 561–564.
[28] H. Long, G. Yang, A.P. Chen, Y.H. Li, P.X. Lu, Growth and characteristics of laser deposited anatase and rutile TiO2 films on Si substrates, Thin Solid Films 517 (2008) 745–749.
[29] T. Ohsaka, F. Izumi, Y. Fujiki, Raman spectrum of anatase, TiO2, Journal of Raman Spectroscopy 7 (1978) 321–324.
[30] A. Li Bassi, D. Cattaneo, V. Russo, C.E. Bottani, E. Barborini, T. Mazza, P. Piseri, P. Milani, F.O. Ernst, K. Wegner, S.E. Pratsinis, Raman spectroscopy characterization of titania nanoparticles produced by flame pyrolysis: the influence of size and stoichiometry, Journal of Applied Physics 98 (2005).
[31] D. Bersani, P.P. Lottici, X.Z. Ding, Phonon confinement effects in the Raman scattering by TiO2 nanocrystals, Applied Physics Letters 72 (1998) 73–75.
[32] R. Wang, N. Sakai, A. Fujishima, T. Watanabe, K. Hashimoto, Studies of surface wettability conversion on TiO2 single-crystal surfaces, Journal of Physical Chemistry B 103 (1999) 2188–2194.
[33] L.Q. Wang, D.R. Baer, M.H. Engelhard, A.N. Shultz, The adsorption of liquid and vapor water on TiO2(110) surfaces: the role of defects, Surface Science 344 (1995) 237–250.
[34] C.M. Woodbridge, X.J. Gu, M.A. Langell, Extra-atomic relaxation energies and auger parameters of titanium compounds, Surface and Interface Analysis 27 (1999) 816–824.
[35] A.F. Carley, P.R. Chalker, J.C. Riviere, M.W. Roberts, The identification and characterisation of mixed oxidation states at oxidised titanium surfaces by analysis of X-ray photoelectron spectra, Journal of the Chemical Society, Faraday Transactions. 1 83 (1987) 351–370.
[36] M. Shirkhanzadeh, XRD and XPS characterization of superplastic TiO2 coatings prepared on Ti6Al4V surgical alloy by an electrochemical method, Journal of Materials Science: Materials in Medicine 6 (1995) 206–210.
[37] E. McCafferty, J.P. Wightman, Determination of the concentration of surface hydroxyl groups on metal oxide films by a quantitative XPS method, Surface and Interface Analysis 26 (1998) 549–564.
[38] A. Podesta, G. Bongiorno, P.E. Scopelliti, S. Bovio, P. Milani, C. Semprebon, G. Mistura, Cluster-assembled nanostructured titanium oxide films with tailored wettability, Journal of Physical Chemistry C 113 (2009) 18264–18269.
[39] C.J. Powell, A. Jablonski, NIST Electron Inelastic-Mean-Free-Path Database — Version 1.1, National Institute of Standards and Technology, Gaithersburg, MD, 2000.
[40] K.C. Prince, V.R. Dhanak, P. Finetti, J.F. Walsh, R. Davis, C.A. Muryn, H.S. Dhariwal, G. Thornton, G. vanderLaan, 2p resonant photoemission study of TiO2, Physical Review B 55 (1997) 9520–9523.
[41] R.L. Kurtz, R. Stock-Bauer, T.E. Msdey, E. Román, J.L. De Segovia, Synchrotron radiation studies of H2O adsorption on TiO2(110), Surface Science 218 (1989) 178–200.
[42] I.D. Cocks, Q. Guo, R. Patel, E.M. Williams, E. Roman, J.L. deSegovia, The structure of TiO2(110) (1×1) and (1×2) surfaces with acetic acid adsorption — a PES study, Surface Science 377 (1997) 135–139.
[43] H. Idriss, V.S. Lusvardi, M.A. Barteau, Two routes to formaldehyde from formic acid on TiO2(001) surfaces, Surface Science 348 (1996) 39–48.
[44] E. Finazzi, C. Di Valentin, G. Pacchioni, Nature of Ti interstitials in reduced bulk anatase and rutile TiO2, Journal of Physical Chemistry C 113 (2009) 3382–3385.
[45] T. Caruso, R.G. Agostino, G. Bongiorno, E. Barborini, P. Piseri, P. Milani, C. Lenardi, S. La Rosa, M. Bertolo, Writing submicrometric metallic patterns by ultraviolet synchrotron irradiation of nanostructured carbon and TiOx–carbon films, Applied Physics Letters 84 (2004) 3.
[46] A.I. Hochbaum, R.K. Chen, R.D. Delgado, W.J. Liang, E.C. Garnett, M. Najarian, A. Majumdar, P.D. Yang, Enhanced thermoelectric performance of rough silicon nanowires, Nature 451 (2008) 163–167.
[47] K. Hashimoto, H. Irie, A. Fujishima, TiO2 photocatalysis: a historical overview and future prospects, Japanese Journal of Applied Physics Part 1-Regular Papers Brief Communications & Review Papers 44 (2005) 8269–8285.
[48] R. Ruus, A. Kikas, A. Saar, A. Ausmees, E. Nommiste, J. Aarik, A. Aidla, T. Uustare, I. Martinson, Ti 2p and O 1s X-ray absorption of TiO2 polymorphs, Solid State Communications 104 (1997) 199–203.
[49] L. Soriano, M. Abbate, J. Vogel, J.C. Fuggle, A. Fernandez, A.R. Gonzalezelipe, M. Sacchi, J.M. Sanz, Chemical-changes induced by sputtering in Tio2 and some selected titanates as observed by X-ray-absorption spectroscopy, Surface Science 290 (1993) 427–435.
[50] B. Poumellec, P.J. Durham, G.Y. Guo, Electronic-structure and X-ray absorption-spectrum of rutile Tio2, Journal of Physics-Condensed Matter 3 (1991) 8195–8204.
[51] A. Tilocca, A. Selloni, Methanol adsorption and reactivity on clean and hydroxylated anatase(101) surfaces, Journal of Physical Chemistry B 108 (2004) 19314–19319.
[52] A. Tilocca, A. Selloni, Structure and reactivity of water layers on defect-free and defective anatase TiO2(101) surfaces, Journal of Physical Chemistry B 108 (2004) 4743–4751.
[53] Y. Li, T. Sasaki, Y. Shimizu, N. Koshizaki, Hexagonal-close-packed, hierarchical amorphous TiO2 nanocolumn arrays: transferability, enhanced photocatalytic activity, and superamphiphilicity without UV irradiation, Journal of the American Chemical Society 130 (2008) 14755–14762.